


# Mixed-metal Ionothermal Synthesis of Metallophthalocyanine Covalent Organic Frameworks for CO<sub>2</sub> Capture and Conversion

## Journal Article

### Author(s):

Song, Kyung Seob; Fritz, Patrick W.; Abbott, Daniel F.; Poon, Lok-Nga; Caridade, Cristiano M.; Gándara, Felipe; [Mougel, Victor](#) ; Coskun, Ali

### Publication date:

2023-09-18

### Permanent link:

<https://doi.org/10.3929/ethz-b-000627413>

### Rights / license:

[Creative Commons Attribution-NonCommercial 4.0 International](#)

### Originally published in:

Angewandte Chemie. International Edition 62(38), <https://doi.org/10.1002/anie.202309775>

### Funding acknowledgement:

853064 - Hybrid Electrocatalysts Inspired by the Nitrogenase Enzyme (EC)



# Mixed-metal Ionothermal Synthesis of Metallophthalocyanine Covalent Organic Frameworks for CO<sub>2</sub> Capture and Conversion

Kyung Seob Song, Patrick W. Fritz, Daniel F. Abbott, Lok Nga Poon, Cristiano M. Caridade, Felipe Gándara, Victor Mougel,\* and Ali Coskun\*

**Abstract:** Phthalocyanines (PCs) are intriguing building blocks owing to their stability, physicochemical and catalytic properties. Although PC-based polymers have been reported before, many suffer from relatively low stability, crystallinity, and low surface areas. Utilizing a mixed-metal salt ionothermal approach, we report the synthesis of a series of metallophthalocyanine-based covalent organic frameworks (COFs) starting from 1,2,4,5-tetracyanobenzene and 2,3,6,7-tetracyanoanthracene to form the corresponding COFs named M-pPPCs and M-anPPCs, respectively. The obtained COFs followed the Irving–Williams series in their metal contents, surface areas, and pore volume and featured excellent CO<sub>2</sub> uptake capacities up to 7.6 mmol g<sup>-1</sup> at 273 K, 1.1 bar. We also investigated the growth of the Co-pPPC and Co-anPPC on a highly conductive carbon nanofiber and demonstrated their high catalytic activity in the electrochemical CO<sub>2</sub> reduction, which showed Faradaic efficiencies towards CO up to 74 % at -0.64 V vs. RHE.

redox properties<sup>[1]</sup> and electrocatalytic activity,<sup>[2]</sup> as the coordinated metal ion can serve as a catalytically active single atom site for various chemical transformations including coupling reactions,<sup>[3]</sup> electrocatalytic transformations such as the electro-reduction of CO<sub>2</sub> to CO or formic acid<sup>[3a,4]</sup> as well as the electrochemical or photochemical reduction of CO<sub>2</sub> to methanol.<sup>[5]</sup> Although small-molecule M-PCs show high potential in these fields, their polymeric counterparts featuring extended conjugated backbones have also gained significant interest as heterogeneous catalysts.<sup>[6]</sup> To this end, PC-containing framework materials such as metal–organic frameworks (MOFs) and covalent organic frameworks (COFs) have also been widely investigated.<sup>[7]</sup> Conventionally most of the PC-based frameworks were prepared using solvothermal methods and, in the case of COFs, mostly systems based on reversible linkages (B–O<sup>[8]</sup> or C=N<sup>[9]</sup>) were reported, while linkages of higher stability resulted in lower crystallinity or amorphous materials.<sup>[10]</sup>

In 2008, Thomas et al. reported an ionothermal approach towards the synthesis of covalent triazine frameworks (CTFs) through the trimerization of 1,4-dicyanobenzene in molten ZnCl<sub>2</sub>.<sup>[11]</sup> Following this report, such ionothermal synthesis approaches have been employed for various cyclization reactions including Zn-PCs, which were obtained as polycrystalline powders with low surface areas.<sup>[12]</sup> More recently, eutectic salt mixtures of ZnCl<sub>2</sub> with various alkali metal salts have also been introduced primarily to achieve lower reaction temperatures for the ionothermal synthesis of porous organic polymers (POPs) and COFs.<sup>[13]</sup> It has also been shown that alkali metal salts can also serve as templates for the synthesis of POPs under ionothermal conditions.<sup>[14]</sup> Considering that M-PCs can be prepared under ionothermal conditions and that small-molecule metal PCs showed exciting catalytic properties,<sup>[3c,12]</sup> we hypothesized that using mixed-metal salt mixtures (MCl<sub>2</sub>/ZnCl<sub>2</sub>) would result in porous polyphthalocyanines (PPCs) with the desired metal ions, given that the complex stability is higher than that of the corresponding Zn-PC according to the Irving–Williams series, which predicts the relative stability of complexes formed by transition metals that increases when moving in the periodic table from Fe<sup>2+</sup> to Cu<sup>2+</sup>.<sup>[15]</sup> In addition, this synthetic approach would also enable a simple tuning of the final material's electric conductivity upon simple introduction of carbon-based materials such as carbon nanotubes and nanofibers, recently shown to enhance the electrocatalytic activity of single-site Fe nitrogen-doped carbon (FeNC)<sup>[16]</sup> and PPC materials.<sup>[17]</sup> Accordingly, herein, we showcased (Figure 1) the effect of mixed-metal

## Introduction

Phthalocyanines (PCs) are naturally occurring nitrogen bridged macrocycles that are well-known for their high chemical and thermal stability and their capability to form stable complexes with metal ions, so-called metallophthalocyanines (M-PCs). M-PCs have been investigated for their

[\*] Dr. K. Seob Song, P. W. Fritz, C. M. Caridade, Prof. Dr. A. Coskun  
 Department of Chemistry, University of Fribourg  
 Chemin du Musée 9, 1700 Fribourg (Switzerland)  
 E-mail: ali.coskun@unifr.ch

Dr. D. F. Abbott, L. Nga Poon, Prof. Dr. V. Mougel  
 Department of Chemistry and Applied Biosciences, ETH Zürich  
 Vladimir-Prelog-Weg 1–5, 8093 Zürich (Switzerland)  
 E-mail: mougelv@ethz.ch

Dr. F. Gándara  
 Department of New Architectures in Materials Chemistry, Materials  
 Science Institute of Madrid–CSIC  
 Sor Juana Inés de la Cruz 3, 28049 Madrid (Spain)

© 2023 The Authors. Angewandte Chemie International Edition published by Wiley-VCH GmbH. This is an open access article under the terms of the Creative Commons Attribution Non-Commercial License, which permits use, distribution and reproduction in any medium, provided the original work is properly cited and is not used for commercial purposes.

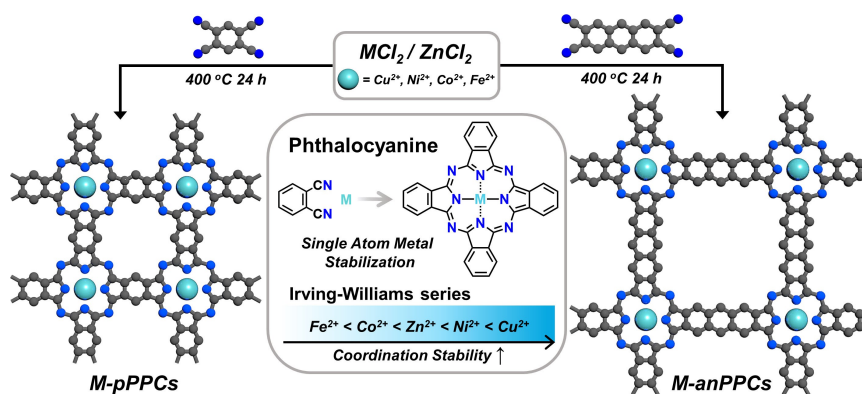


**Figure 1.** Schematic representation of the mixed-metal salt approach towards the synthesis of metallophthalocyanine covalent organic frameworks starting from 1,2,4,5-tetracyanobenzene and 2,3,6,7-tetracyanoanthracene. Inset: Phthalocyanine formation and the stability of the bivalent transition metal complexes following the Irving–Williams Series.

salt compositions ( $MCl_2/ZnCl_2$ ,  $M=Cu^{2+}$ ,  $Ni^{2+}$ ,  $Co^{2+}$  and  $Fe^{2+}$ ) in the ionothermal synthesis of PPCs. Notably, we observed a direct correlation between the Irving–Williams series and the metal contents, surface areas and  $CO_2$  uptake capacities of PPCs, thus offering a highly tunable approach to control the properties of these polymers. The polymers showed high surface areas up to  $2043\text{ m}^2\text{ g}^{-1}$  and  $CO_2$  uptake capacities up to  $7.6\text{ mmol g}^{-1}$  at 273 K, 1.1 bar. In order to explore their catalytic properties and demonstrate the potential of M-PPCs in both  $CO_2$  capture and conversion, we showed that the Co-based PPCs can also be used as highly efficient electrocatalysts for the  $CO_2$  reduction reaction once combined with highly conductive carbon nanofibers (CNFs).

## Results and Discussion

Metallophthalocyanine-based COFs were prepared (Figure 1) starting from 1,2,4,5-tetracyanobenzene and 2,3,6,7-tetracyanoanthracene to form the corresponding polymers named M-pPPCs and M-anPPCs, respectively, under ionothermal conditions employing various metal salt mixtures ( $MCl_2/ZnCl_2$ ,  $M=Cu^{2+}$ ,  $Ni^{2+}$ ,  $Co^{2+}$  and  $Fe^{2+}$ ) at  $400^\circ\text{C}$ . The

metal contents of the PPCs were analyzed (Table 1) by inductively coupled plasma optical emission spectroscopy (ICP-OES) measurements. The metal contents of M-pPPCs and M-anPPCs nicely followed the Irving–Williams series. Cu-, Ni-, Co- and Fe-pPPCs exhibited 4.83 wt% of Cu, 2.62 wt% of Ni, 0.32 wt% of Co and 0.19 wt% of Fe (Table 1), respectively and Zn contents in the range of 0.02–0.52 wt%. On the other hand, M-anPPCs showed significantly lower amounts of metal ions. We observed 0.22 wt% of Cu, 0.11 wt% of Ni, 0.098 wt% of Co and 0.05 wt% of Fe for Cu-, Ni-, Co- and Fe-anPPC, respectively, and also Zn contents in the range of 0.02–0.12 wt%. The presence of  $Zn^{2+}$  in the PPCs suggests the formation of Zn-PPC (Figure S1) and subsequent exchange with the second metal ion, provided that the complex stability is higher than that of Zn-PPC according to the Irving–Williams series. Accordingly, as the complex stability decreased, we observed higher  $Zn^{2+}$  contents in the resulting PPCs. Additionally, as a model reaction, 1,2-dicyanobenzene and metal salt mixtures ( $MCl_2/ZnCl_2$ ,  $M=Cu^{2+}$ ,  $Ni^{2+}$ ,  $Zn^{2+}$ ,  $Co^{2+}$  and  $Fe^{2+}$ ) were also reacted under ionothermal conditions at  $400^\circ\text{C}$  (Figure S2). Elemental analysis (EA) was performed to probe the elemental compositions of M-pPPCs and M-anPPCs (Table S1 and Table S2). EA results of M-pPPCs were found to

**Table 1:** Porosity analysis of M-pPPCs and M-anPPCs along with their metal contents.

	BET <sup>[a]</sup> ( $\text{m}^2\text{ g}^{-1}$ )	$S_{\text{micro}}^{\text{[b]}}$ ( $\text{m}^2\text{ g}^{-1}$ )	$S_{\text{ext}}$ ( $\text{m}^2\text{ g}^{-1}$ )	$V_{\text{total}}^{\text{[c]}}$ ( $\text{cm}^3\text{ g}^{-1}$ )	$V_{\text{micro}}^{\text{[d]}}$ ( $\text{cm}^3\text{ g}^{-1}$ )	$V_{\text{external}}^{\text{[e]}}$ ( $\text{cm}^3\text{ g}^{-1}$ )	Metal <sup>[f]</sup> (wt%)	Zinc <sup>[f]</sup> (wt%)
Cu-pPPC	579	545	34	0.29	0.24	0.05	4.83	0.16
Ni-pPPC	162	145	17	0.10	0.07	0.03	2.62	0.52
Co-pPPC	159	145	14	0.08	0.06	0.02	0.32	0.19
Fe-pPPC	5.8	2.0	3.8	0.0084	0.0013	0.0071	0.19	0.04
Zn-pPPC	5.9	1.3	4.6	0.0076	0.0002	0.0074	–	0.51
Cu-anPPC	2043	2003	40	0.94	0.86	0.08	0.22	0.12
Ni-anPPC	1401	1328	73	0.67	0.56	0.11	0.11	0.09
Co-anPPC	1356	1304	52	0.62	0.54	0.08	0.098	0.02
Fe-anPPC	1054	1013	41	0.49	0.43	0.06	0.05	0.04

[a] BET surface area calculated over the relative pressure range ( $P/P_0$ ) of 0.01–0.11. [b] Micropore surface area calculated using the  $t$ -plot method. [c] Total pore volume obtained at  $P/P_0=0.99$ . [d] Micropore volume calculated using the  $t$ -plot method. [e]  $V_{\text{external}}=V_{\text{total}}-V_{\text{micro}}$ . [f] Metal content is obtained by ICP-OES.

be in a good agreement with the calculated values. M-anPPCs, however, showed lower heteroatom contents as it is commonly observed for the polymers synthesized under ionothermal conditions. We observed consistently lower metal contents for all the polymers with respect to the theoretically attainable metal contents owing to the fact that only 2 wt%  $MCl_2$  was used in the salt mixture ( $MCl_2/ZnCl_2$ ) to prevent metal nanoparticle formation. Moreover, we observed significantly lower metal contents for M-anPPCs in line with their lower nitrogen contents. Both M-pPPCs and M-anPPCs showed the co-existence of M-PC and  $H_2PC$  in the polymer networks. Thermogravimetric analysis (TGA) of M-pPPCs and M-anPPCs were performed under air and nitrogen atmospheres (Figure S3). All the polymers (Figure S3a and Figure S3c) were found to be thermally stable up to  $500^\circ C$  under air atmosphere except for Fe-pPPC and Fe-anPPC, suggesting a lower degree of polymerization, which may be associated with the low complex stability of Fe(II). These findings further suggest that the growth of PPCs involves a dynamic metal exchange process, that is the exchange of  $Zn^{2+}$  with the secondary metal ions, and effects the degree of polymerization in line with the stability of metal complexes. In order to probe the crystallinity of M-pPPCs and M-anPPCs, powder X-ray diffraction (PXRD) analysis was conducted (Figure S4). All M-pPPCs showed a rather good crystallinity. M-pPPCs featured distinct reflections at  $2\theta$   $8.6^\circ$  and  $26^\circ$ . Structure models were created and geometrically optimized with energy minimization procedures, based on the formation of extended square layers (**sql**), with eclipsed stacking (atomic coordinates in Table S3 for Ni-pPPC and Table S4 for Ni-anPPC, representation in Figure S5). As shown in Figure S4, the simulated diffractogram matches well with the observed diffractions, wherein the reflection at  $8.6^\circ$  corresponds to the (100) plane and the one at  $26^\circ$  to the (001) plane, indicative of the interlayer distance of  $3.4 \text{ \AA}$ . Cu- and Ni-pPPC showed higher crystallinity compared to the Co- and Fe-pPPC, indicating the impact of metal complex stabilities on the crystallinity of M-pPPCs under ionothermal conditions. M-anPPCs on the other hand showed lower crystallinity compared to M-pPPCs. Cu- and Ni-anPPCs exhibited broader features at  $5.9^\circ$  and  $5.7^\circ$ , respectively, indicating the presence of a long-range order, albeit with lower crystallinity and agrees well with the simulated pattern of Ni-anPPC (Figure S4b). Scanning electron microscopy (SEM) analysis of Cu-PPCs revealed (Figure S6 and Figures7) the presence of stacked two-dimensional sheets consistent with the PXRD results and proposed crystal models. SEM energy dispersive X-ray analysis (SEM-EDX) analysis showed uniformly distributed metal ions ( $Cu^{2+}$ ,  $Ni^{2+}$ ,  $Co^{2+}$  and  $Fe^{2+}$ ) on the surface of PPCs (Figure S8 and Figure S9).

In order to prove the formation of PPCs, Fourier transform infrared spectroscopy (FT-IR) analysis was performed (Figure S10). Full conversion of the precursors can be verified by the disappearance of the -CN stretching band at around  $2220 \text{ cm}^{-1}$ . The characteristic C-N stretching modes at  $1481$  and  $1256 \text{ cm}^{-1}$  corresponding to the pyrrole ring of PC were also clearly observed. Importantly, we also observed PC-metal bonding (M-N) in the range of  $896-$

$908 \text{ cm}^{-1}$ .<sup>[18]</sup> Whereas these modes were well-defined in the M-pPPCs, the M-anPPCs showed much broader features, likely due to the  $\pi$ -extended nature of the polymer backbone. In order to further investigate the formation of the PPCs, UV/Vis spectra were recorded (Figure 2 and Figure S11). PCs typically show two absorption bands, namely, Q-band and Soret-band. Whereas the Q-band appears around  $600-700 \text{ nm}$  arising from degenerated electronic transition from the ground state ( $S_0$ ) to the first excited state ( $S_1$ ), the Soret-band (also referred to as B-band) appears around  $300-350 \text{ nm}$  owing to the electronic transition from the ground state ( $S_0$ ) to the second excited state ( $S_2$ ). While the M-pPPCs featured both Q- and Soret-bands indicating the successful formation of PCs, the  $\pi$ -extended M-anPPCs did not show Q-band owing to the stronger  $\pi-\pi$  stacking interactions between the layers (Figure 2), which is often observed in the thin-film PPCs and PC aggregates.<sup>[19]</sup> The UV/Vis diffuse reflectance spectra on the other hand exhibited Q-bands for all the polymers (Figure S11). The evolution of UV/Vis spectra going from 1,2,4,5-tetracyano benzene to Cu-pPPC (Figure S12) exhibited the phthalocyanine formation and peak broadening upon polymerization.

The chemical composition and the coordination environment of the metal species in the PPCs were investigated using X-ray photoelectron spectroscopy (XPS) analysis (Figures 3 and 4, Figures S13–S15 and Table S5). The N1s XPS spectra of the M-pPPCs and M-anPPCs showed the characteristic bridging aza-nitrogens (denoted as N1) at around  $400 \text{ eV}$  and the N-moieties of the pyrrole units (N2)

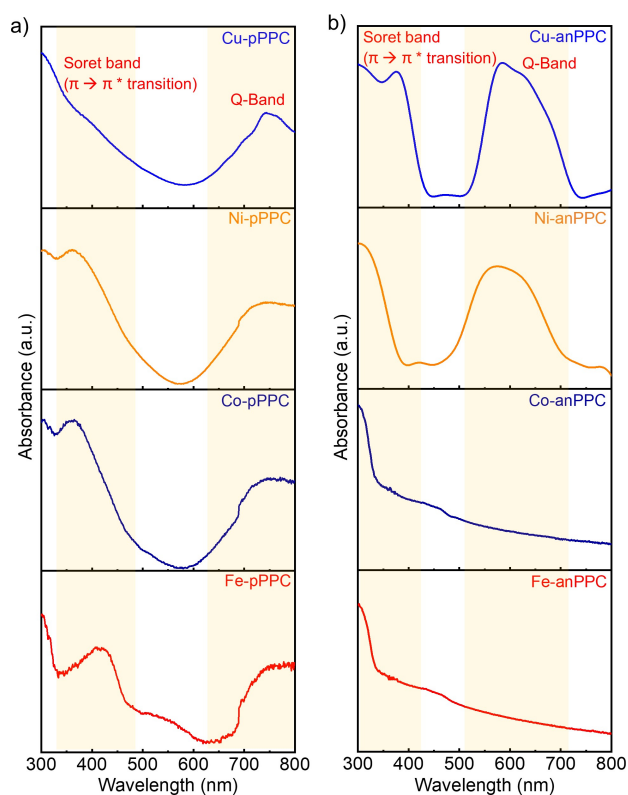


**Figure 2.** Solid-state UV/Vis spectra of a) M-pPPCs and b) M-anPPCs ( $M=Cu^{2+}$ ,  $Ni^{2+}$ ,  $Co^{2+}$  and  $Fe^{2+}$ ).



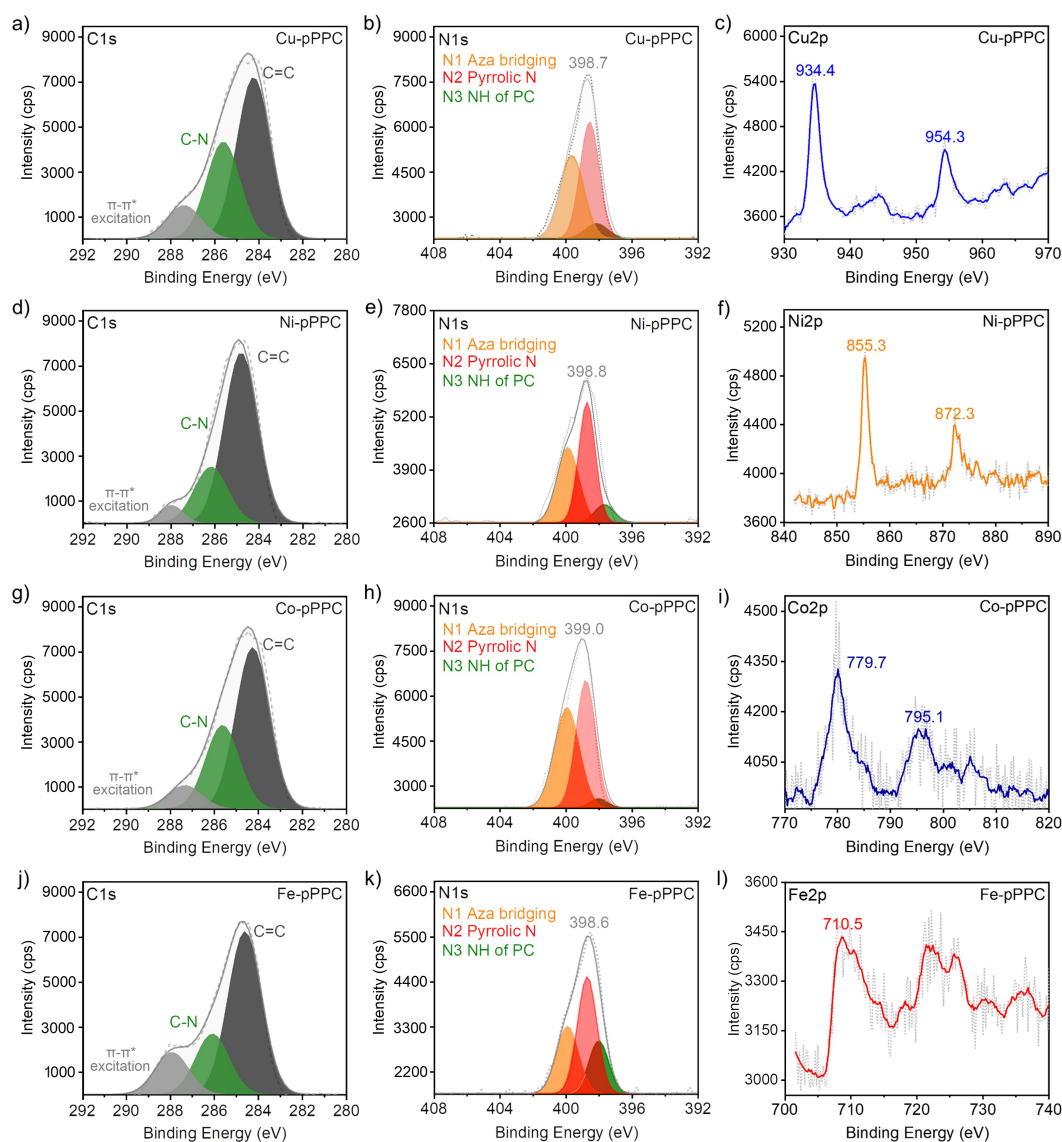


**Figure 3.** XPS analysis of M-pPPCs ( $M=\text{Cu}^{2+}$ ,  $\text{Ni}^{2+}$ ,  $\text{Zn}^{2+}$ ,  $\text{Co}^{2+}$  and  $\text{Fe}^{2+}$ ). The deconvoluted C1s (a, d, g, j), N1s (b, e, h, k) and Metal 2p (c, f, i, l) spectra of M-pPPCs, verifying the formation of PC moieties.

at around 399 eV.<sup>[20]</sup> M-pPPCs and M-anPPCs also featured small contributions from N–H functionalities (N3) at 398 eV, indicating that non-metallated PC moieties were also present in the polymers.<sup>[20]</sup> Interestingly, in the case of the M-anPPCs, a significant increase in the intensity of N3 peak can be observed when using metal ions with lower coordination stability relative to  $\text{Zn}^{2+}$  in the Irving–Williams Series, namely  $\text{Co}^{2+}$  and  $\text{Fe}^{2+}$ . We also investigated the local coordination environment of the metal ions. Cu-pPPC showed narrow peaks at 934.4 eV ( $2p_{3/2}$ ) and a satellite peak at 954.3 eV ( $2p_{1/2}$ ) indicating that divalent Cu species are present in a Cu- $\text{N}_4$  environment (Figure 3).<sup>[21]</sup> Similarly, Ni-pPPC showed the characteristic peaks at 855.3 and 872.3 eV ( $2p_{3/2}$  and  $2p_{1/2}$  respectively) entailing a well-defined coordination environment for  $\text{Ni}^{2+}$  as Ni- $\text{N}_4$ .<sup>[22]</sup> Co-pPPC exhibited broad and low intensity peaks at 779.7 eV ( $2p_{3/2}$ ) and 795.1 eV ( $2p_{1/2}$ ).<sup>[23]</sup> Similar to Co-pPPC, Fe-pPPC also

showed broad and low intensity peaks at 710.5 eV,<sup>[24]</sup> suggesting a poorly defined coordination environment. Compared to the M-pPPCs, the peak intensities in the XPS spectra of M-anPPCs were lower owing to the lower metal contents (Figure 4). Consistent with Cu- and Ni-pPPC, Cu-anPPC and Ni-anPPC also showed distinctive features in the Cu2p (933.5 eV and 953.7 eV) and Ni2p (855.4 eV and 872.6 eV) spectra, without any satellites, confirming a well-defined coordination environment. Co-anPPC on the other hand showed a broad peak at 780.5 eV and strong satellites pointing towards a poor coordination environment. Interestingly, Fe-anPPC did not show any peak in the Fe2p range due to extremely low Fe content, which is expected considering the lower complex stability of  $\text{Fe}^{2+}$  in the Irving–Williams Series relative to  $\text{Zn}^{2+}$ . In addition, we also performed XPS analysis of Zn-pPPC (Figure S15). N1s (Figure S15b) spectrum of Zn-pPPC revealed the presence

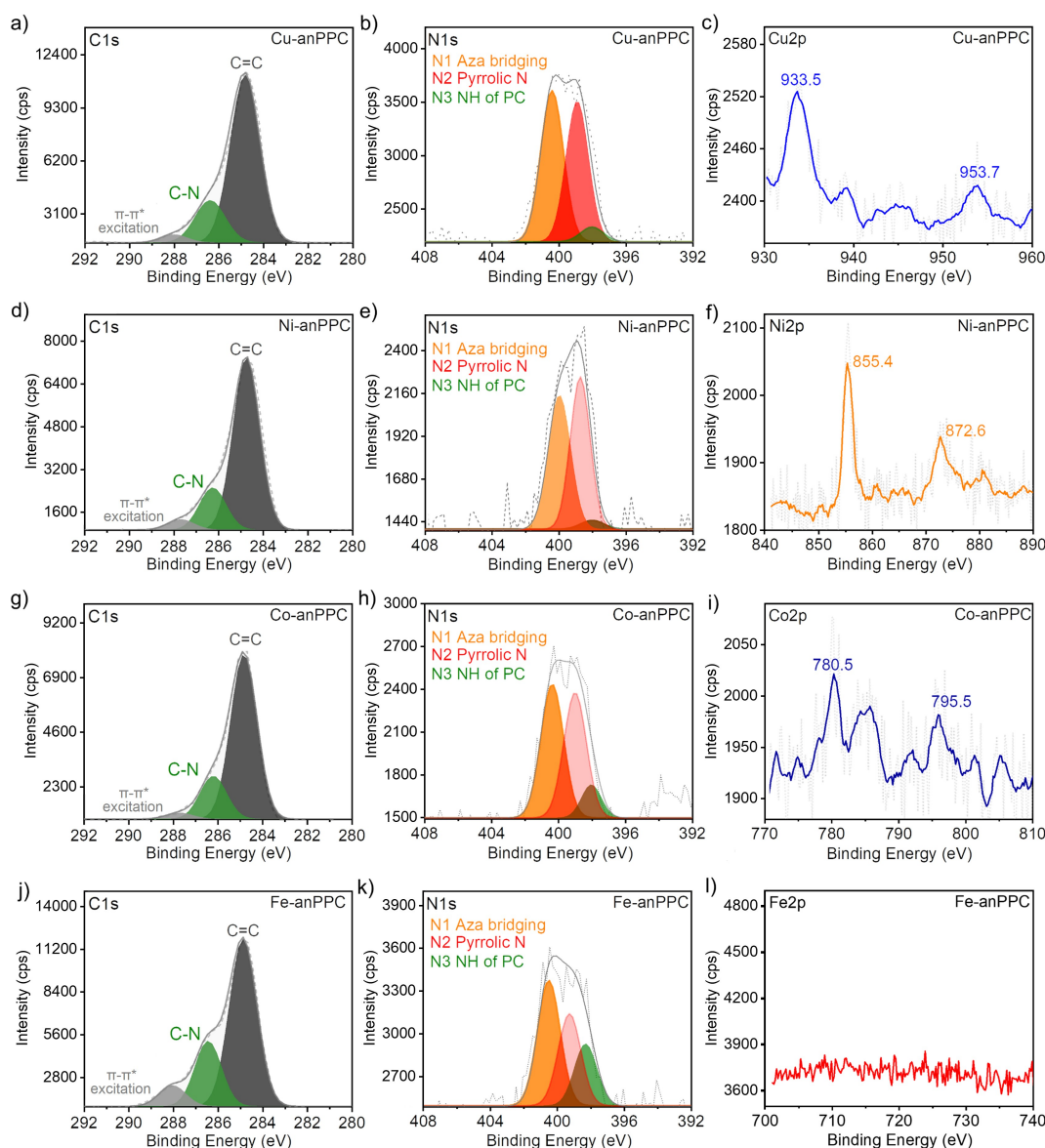


**Figure 4.** XPS analysis of M-anPPCs ( $M=\text{Cu}^{2+}$ ,  $\text{Ni}^{2+}$ ,  $\text{Zn}^{2+}$ ,  $\text{Co}^{2+}$  and  $\text{Fe}^{2+}$ ). The deconvoluted C1s (a, d, g, j), N1s (b, e, h, k) and Metal 2p (c, f, i, l) spectra of M-anPPCs, verifying the formation of PC moieties.

of N1, N2 along with N3, which corresponds to the  $\text{H}_2\text{PC}$ .<sup>[25]</sup> Generally, N1/N2 ratios of PPCs were found to be 1, however, this ratio was 0.6 in the case of Zn-pPPC owing to significantly higher  $\text{H}_2\text{PC}$  content (See Table S5).<sup>[25]</sup> The local coordination environment of Zn-pPPC showed Zn- $\text{N}_4$  (Figure S15c) with narrow peaks at 1021.4 eV ( $2p_{3/2}$ ) and 1044.1 eV ( $2p_{1/2}$ ).<sup>[26]</sup> Importantly, Zn-pPPC showed the lowest metal content of 0.51 wt% Zn and mainly  $\text{H}_2\text{PC}$  moieties (See Table 1) owing to its low complex stability.

We investigated the effect of the mixed-metal approach on the textural properties of PPCs, Brunauer–Emmett–Teller (BET) surface area analysis of PPCs using Ar at 77 K was performed (Figure 5a, Figure 5d, Table 1 and Figure S16, Figure S17, Figure S18). Cu-, Ni-, and Co-pPPCs showed type I isotherms, indicating the presence of abundant micropores, whereas Zn- and Fe-pPPCs were found to

be nonporous. The BET model, for which the valid pressure ranges were obtained from the Rouquerol plots (Figure S16), resulted in the BET surface areas of 579, 162, 159, 5.8 and  $5.9 \text{ m}^2 \text{ g}^{-1}$  for Cu-pPPC, Ni-pPPC, Co-pPPC, Fe-pPPC and Zn-pPPC, respectively (Figure 5a and Table 1). Notably, BET surface areas followed the complex stabilities predicted by the Irving–Williams series. Accordingly, Irving–Williams series trend is also observed in the pore-size distribution (PSD). Cu- and Ni-pPPCs exhibited micropores at around 0.5 nm and a second pore around 0.9 nm (Figure S18). Overall, the pore volume decreased going from Cu-pPPC to Co-pPPC (Table 1). The trend in surface area, PSD and pore volume becomes even more apparent in the case of M-anPPCs. M-anPPCs also showed type I isotherms, highly microporous structures, and exceptionally high surface areas of 2043, 1401, 1356 and  $1054 \text{ m}^2 \text{ g}^{-1}$  for Cu-anPPC,

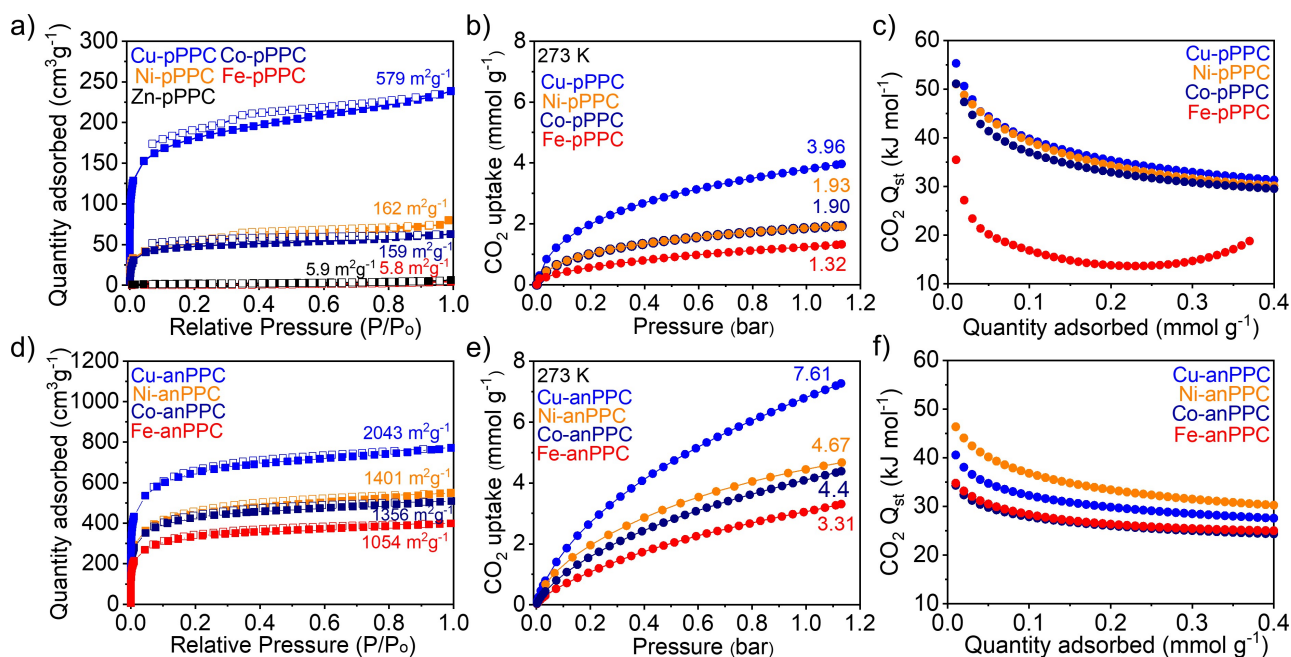


**Figure 5.** BET surface area analysis of a) metallophthalocyanine-based COFs synthesized from 1,2,4,5-tetracyanobenzene (M-pPPCs) and d) 2,3,6,7-tetracyanoanthracene (M-anPPCs) at 77 K using Ar. CO<sub>2</sub> adsorption isotherms of b) M-pPPCs and e) M-anPPCs at 273 K up to 1.1 bar. CO<sub>2</sub> heat of adsorption ( $Q_{st}$ ) of c) M-pPPCs and f) M-anPPCs calculated from CO<sub>2</sub> isotherms recorded at 273, 298 and 323 K.

Ni-anPPC, Co-anPPC and Fe-anPPC, respectively (Figure 5d and Table 1), which were calculated based on the BET linear plots and Roquerol plots (Figure S17). The BET surface area of Cu-anPPC, 2043 m<sup>2</sup>g<sup>-1</sup>, to the best of our knowledge, is the highest surface area among the reported porphyrin- and phthalocyanine-based POPs and COFs.<sup>[27]</sup> Due to the larger size of the anthracene monomer, the M-anPPCs formed larger pores around 0.6, 0.9 and 1.4 nm (Figure S18). The pore volumes of the M-anPPCs were also significantly higher than those of the M-pPPCs (Table 1) and followed the Irving–Williams complex stability series.

The promising sorption properties of PPCs prompted us to investigate their CO<sub>2</sub> uptake capacities at 273, 298, and 323 K (Figure S19 and Table S6, Figure S20 and Table S7). The M-pPPCs exhibited CO<sub>2</sub> uptake capacities of 3.96 mmol g<sup>-1</sup> for Cu-pPPC, 1.93 mmol g<sup>-1</sup> for Ni-pPPC, 1.90 mmol g<sup>-1</sup> for Co-pPPC, and 1.32 mmol g<sup>-1</sup> for Fe-pPPC at 273 K, 1.1 bar following the same trend in their surface areas (Figure 5b and 5a). Moreover, the heat of adsorption ( $Q_{st}$ ) values for CO<sub>2</sub> (Figure 5c and Table S6) were found to be in the range of 55.3–51.1 kJ mol<sup>-1</sup> at zero coverage for Cu-, Ni-, and Co-pPPC, which falls into the range of chemisorption. However, looking at the desorption branches of the isotherms, all CO<sub>2</sub> uptake isotherms were fully reversible. High CO<sub>2</sub> affinity of M-pPPCs was attributed to the presence of metal ions along with the high micropore contents (94 % of Cu-pPPC, 89.5 % of Ni-pPPC, 92.0 % of Co-pPPC). Fe-pPPC exhibited a relatively low  $Q_{st}$  value of 35.5 kJ mol<sup>-1</sup> at zero coverage that drastically drops at high CO<sub>2</sub> loadings owing to its extremely low surface area (5.8 m<sup>2</sup>g<sup>-1</sup>) and the poorly defined Fe-N<sub>4</sub> coordination environment (Figure 5a and Figure 31). In agreement with

the higher surface areas of the M-anPPCs compared to the M-pPPCs, CO<sub>2</sub> uptake capacities were found to be significantly higher (Figure 5e). Especially, Cu-anPPC showed an outstanding CO<sub>2</sub> uptake capacity of 7.61 mmol g<sup>-1</sup> at 273 K and 1.1 bar (Table S7). M-anPPCs showed lower  $Q_{st}$  values in the range of 46.3–34.7 kJ mol<sup>-1</sup> at zero coverage (Figure 5f and Table S7). Comparing the  $Q_{st}$  values for the M-anPPCs with those of M-pPPCs, it became clear that the overall lower values of the M-anPPCs are likely due to their lower metal contents (Table 1).

Porous materials capable of capturing and converting CO<sub>2</sub> into value added products are of great interest. Considering the recent reports of Co-based PC electrocatalysts for CO<sub>2</sub> electroreduction,<sup>[4a,28]</sup> we further investigated the catalytic performances of Co-pPPC and Co-anPPC. Initial catalytic studies of the PPCs revealed that their low electrical conductivity was highly detrimental to their catalytic activity, with high resistances resulting in high overpotentials and low catalytic currents (Figure S21a). In addition, cyclic voltammetry (CV) analysis revealed that the materials undergo significant changes upon potential cycling (Figure S21b). In order to circumvent these limitations, we explored the incorporation of CNFs in the PPCs.<sup>[17]</sup> We have previously shown that while CNFs yield almost exclusively H<sub>2</sub> (>90 %) at CO<sub>2</sub>RR-relevant potentials (e.g. <−0.7 V), they can drastically increase the CO<sub>2</sub>RR performance of electrocatalysts due to their high conductivity, hydrophobicity, and large specific surface area.<sup>[16]</sup> Accordingly, we performed the synthesis of Co-pPPC and Co-anPPC by including CNFs in the reaction mixture, thus forming more conductive, crystalline Co-pPPC@CNFs and Co-anPPC@CNFs with higher metal contents compared to the



ones without CNFs (see Supporting Information for synthesis details and product characterization and CO<sub>2</sub> adsorption analysis, Figure S22–S29, Table S8–S10). Co-pPPC@CNFs and Co-anPPC@CNFs showed BET surface areas of 713 and 528 m<sup>2</sup>g<sup>-1</sup> (Figure S28 and Table S8) along with the metal contents of 0.51 and 1.85 wt%, respectively. These results suggest that CNFs act as a structural template for the growth of PPCs, thus enabling higher surface areas and improved crystallinity (Figure S24). A direct comparison of the linear sweep voltammograms (LSVs) for the CNF-supported PPCs versus the unsupported PPCs showed that catalytic current densities more than doubled upon incorporation of CNFs (Figure S30). The LSVs of Co-pPPC@CNFs and Co-anPPC@CNFs recorded in Ar-saturated and CO<sub>2</sub>-saturated 0.5 M KHCO<sub>3</sub> are compared in Figure 6a. For both materials, it is observed that higher current densities were achieved at low to intermediate overpotentials in CO<sub>2</sub>-saturated electrolyte vs Ar-saturated one. Furthermore, the current densities achieved in Ar-saturated electrolyte become greater as the overpotential is increased. These distinct differences in the LSV profiles suggest that the materials are active towards CO<sub>2</sub>RR, but the hydrogen evolution reaction (HER) becomes more competitive at high overpotentials.

In order to further explore the electrocatalytic activity of Co-pPPC@CNFs and Co-anPPC@CNFs, chronoamperometry (CA) was performed at potentials ranging from -0.44 to -1.04 V vs. RHE (Figure S31). Stable current profiles were obtained over the course of each 45 minutes potential hold except at -1.04 V on Co-pPPC@CNFs. The steadily decreasing current observed at this potential suggests that Co-pPPC@CNFs is unstable at high overpotentials and may degrade into a more HER-active material, e.g. Co nanoparticles. In all cases, however, on-line gas chromatography confirmed that CO and H<sub>2</sub> were the only major gas-phase products. This is in good agreement with recent studies on CoPc-based catalysts, which report CO as the sole CO<sub>2</sub>RR product.<sup>[28a,29]</sup> This suggests that CO<sub>2</sub>RR on our CNF-supported materials proceeds through a similar reduction pathway, in which CO<sub>2</sub> is adsorbed to the Co active center and is reduced to COOH\* and subsequently to CO\* before

being desorbed, with the formation of COOH\* serving as the rate determining step.<sup>[29b]</sup>

The Faradaic efficiencies of the CNF-supported PPCs towards CO (FE<sub>CO</sub>) and H<sub>2</sub> (FE<sub>H<sub>2</sub></sub>) are compared as a function of the applied potential in Figure 6b. We observed that Co-pPPC@CNFs displayed FEs towards CO between 58–74% within a potential range of -0.44 to -0.84 V, after which point the selectivity shifts almost exclusively to HER. On the other hand, Co-anPPC@CNFs reached a peak with 67% FE<sub>CO</sub> at -0.84 V and maintained a moderate FE of 41% even at the highest overpotential examined. In general, Co-pPPC@CNFs showed better CO<sub>2</sub>RR performance at low overpotentials (-0.44 to -0.64 V<sub>RHE</sub>) while Co-anPPC@CNFs showed better selectivity and activity at intermediate to high potentials (≤ -0.84 V<sub>RHE</sub>). The better performance of Co-anPPC@CNFs with increasing potential is also reflected in the partial current densities towards CO (*j*<sub>CO</sub>) (Figure 6c). While both materials display comparable *j*<sub>CO</sub> until ca. -0.84 V, the partial current density of Co-anPPC@CNFs increases to -7.5 mA cm<sup>-2</sup> at -1.04 V, which is 5 times higher than that of Co-pPPC@CNFs. The higher selectivity and activity of Co-anPPC@CNFs was attributed to the significantly higher metal content and to the consequent higher availability of CO<sub>2</sub> molecules in the polymer network. When compared to the recent literature reports, we find that the FE<sub>CO</sub> is in a similar range (See Table S11) as reported CoPc materials e.g., 68% FE<sub>CO</sub> at -0.63 V for CoPc's linked by Cu nodes; 81% FE<sub>CO</sub> at -0.69 V for CoPc on chemically converted graphene<sup>[30]</sup> 72% FE<sub>CO</sub> at -0.68 V for CoTPP on CNTs.<sup>[31]</sup> In addition, we find that the Co-PPCs@CNFs are recyclable, such that their FE<sub>CO</sub> is maintained over the course of several CA measurements (Figure S32). Comparison of the Co 2p XPS spectra for the electrodes after the first electrolysis cycle and the last electrolysis cycle also reveal that the Co active centers experience negligible changes over the course of several cycles (Figure S33).

Overall, the electrochemical results presented above demonstrate that a drastic improvement in electrochemical activity is obtained upon synthesizing the Co-PPCs directly onto the CNFs support. Further optimization of the Co-PPC@CNF content and the electrode preparation protocol

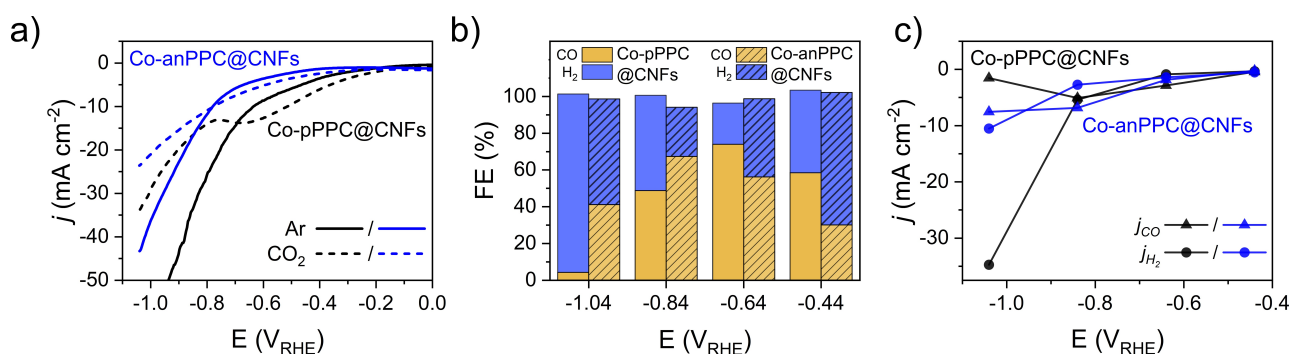


**Figure 6.** a) Linear sweep voltammograms of Co-pPPC@CNFs and Co-anPPC@CNFs recorded at 5 mV s<sup>-1</sup> in Ar and CO<sub>2</sub>-saturated 0.5 M KHCO<sub>3</sub> electrolyte, b) Faradaic efficiencies towards CO and H<sub>2</sub> for Co-pPPC@CNFs and Co-anPPC@CNFs at the designated potentials, and c) the CO and H<sub>2</sub> partial current densities as a function of the applied potential.



has the potential to lead to highly active and competitive CO<sub>2</sub>RR catalysts with a high selectivity towards CO. Moreover, this facile synthetic approach can easily be extended to the other M-pPPC and M-anPPCs in the series to produce highly conductive electrocatalytic materials for various catalytic applications.

## Conclusion

We demonstrated that metallophthalocyanine-based covalent organic frameworks follow the Irving-Williams series in terms of their metal contents, surface areas and pore volumes under mixed-metal ionothermal conditions, thus offering a versatile and highly tunable platform to synthesize various COFs while also expanding the scope of ionothermal synthesis. The resulting COFs showed exceptional CO<sub>2</sub> uptake capacities and were used as efficient electrocatalysts for the CO<sub>2</sub> reduction reaction when paired with carbon nanofibers. Altogether, these results highlight the potential of the mixed-metal ionothermal approach for the synthesis of fully conjugated COFs for CO<sub>2</sub> capture and conversion.

## Acknowledgements

This publication was created as a part of NCCR Catalysis (grant number 180544), a National Center of Competence in Research funded by the Swiss National Science Foundation. A.C. also acknowledges that the preliminary results of this study were obtained with the support from the Swiss National Science Foundation (SNF), 200021-175947. V.M. and D. A. thank the European Research Council (ERC) under the European Union's Horizon 2020 research and innovation program (Grant Agreement No. 853064). Microscopy was performed on equipment provided by the Adolphe Merkle Institute, University of Fribourg, Switzerland. Open Access funding provided by Université de Fribourg.

## Conflict of Interest

The authors declare no conflict of interest.

## Data Availability Statement

The data that support the findings of this study are available from the corresponding author upon reasonable request.

**Keywords:** CO<sub>2</sub> Capture · Covalent Organic Frameworks · Electrocatalysis · Ionothermal Synthesis · Phthalocyanine

- [1] a) A. Lever, *J. Porphyrins Phthalocyanines* **1999**, *3*, 488; b) E. Milaeva, G. Speier, A. Lever, *The phthalocyanines, Properties and Applications*, Vol. 2, **1992**, pp. 1-66. <https://apps.dtic.mil/sti/citations/ADA251744>.

- [2] S. Yang, Y. Yu, X. Gao, Z. Zhang, F. Wang, *Chem. Soc. Rev.* **2021**, *50*, 12985.
- [3] a) Z. Yue, C. Ou, N. Ding, L. Tao, J. Zhao, J. Chen, *ChemCatChem* **2020**, *12*, 6103; b) J. H. Zagal, S. Griveau, J. F. Silva, T. Nyokong, F. Bedioui, *Coord. Chem. Rev.* **2010**, *254*, 2755; c) A. B. Sorokin, *Chem. Rev.* **2013**, *113*, 8152.
- [4] a) M. Wang, K. Torbensen, D. Salvatore, S. Ren, D. Joulié, F. Dumoulin, D. Mendoza, B. Lassalle-Kaiser, U. Işci, C. P. Berlinguette, *Nat. Commun.* **2019**, *10*, 3602; b) H. Zhao, Y. Zhang, B. Zhao, Y. Chang, Z. Li, *Environ. Sci. Technol.* **2012**, *46*, 5198; c) X. Zhang, Z. Wu, X. Zhang, L. Li, Y. Li, H. Xu, X. Li, X. Yu, Z. Zhang, Y. Liang, *Nat. Commun.* **2017**, *8*, 14675.
- [5] a) Y. Wu, Z. Jiang, X. Lu, Y. Liang, H. Wang, *Nature* **2019**, *575*, 639; b) X. Liu, B.-Q. Li, B. Ni, L. Wang, H.-J. Peng, *J. Energy Chem.* **2022**, *64*, 263.
- [6] a) N. B. McKeown, *J. Mater. Chem.* **2000**, *10*, 1979; b) S. Lin, C. S. Diercks, Y.-B. Zhang, N. Kornienko, E. M. Nichols, Y. Zhao, A. R. Paris, D. Kim, P. Yang, O. M. Yaghi, *Science* **2015**, *349*, 1208.
- [7] S. De, T. Devic, A. Fateeva, *Dalton Trans.* **2021**, *50*, 1166.
- [8] E. L. Spitzer, W. R. Dichtel, *Nat. Chem.* **2010**, *2*, 672.
- [9] M. Wang, M. Ballabio, M. Wang, H.-H. Lin, B. P. Biswal, X. Han, S. Paasch, E. Brunner, P. Liu, M. Chen, *J. Am. Chem. Soc.* **2019**, *141*, 16810.
- [10] a) S. Huang, K. Chen, T.-T. Li, *Coord. Chem. Rev.* **2022**, *464*, 214563; b) M. Chen, H. Li, C. Liu, J. Liu, Y. Feng, A. G. Wee, B. Zhang, *Coord. Chem. Rev.* **2021**, *435*, 213778.
- [11] P. Kuhn, M. Antonietti, A. Thomas, *Angew. Chem. Int. Ed.* **2008**, *47*, 3450.
- [12] P. Kuhn, A. Thomas, M. Antonietti, *Macromolecules* **2009**, *42*, 319.
- [13] J. Maschita, T. Banerjee, G. Savasci, F. Haase, C. Ochsenfeld, B. V. Lotsch, *Angew. Chem. Int. Ed.* **2020**, *59*, 15750.
- [14] K. S. Song, S. N. Talapaneni, T. Ashirov, A. Coskun, *ACS Appl. Mater. Interfaces* **2021**, *13*, 26102.
- [15] H. Irving, R. Williams, *J. Chem. Soc.* **1953**, 3192.
- [16] D. Karapinar, N.-H. Tran, D. Giaume, N. Ranjbar, F. Jaouen, V. Mougél, M. Fontecave, *Sustain. Energy Fuels* **2019**, *3*, 1833.
- [17] D. Karapinar, A. Zitolo, T. N. Huan, S. Zanna, D. Taverna, L. H. Galvão Tizei, D. Giaume, P. Marcus, V. Mougél, M. Fontecave, *ChemSusChem* **2020**, *13*, 173.
- [18] a) T. Kobayashi, F. Kurokawa, N. Uyeda, E. Suito, *Spectrochim. Acta* **1970**, *26*, 1305; b) Z. Liu, X. Zhang, Y. Zhang, J. Jiang, *Spectrochim. Acta Part A* **2007**, *67*, 1232.
- [19] a) V. I. Korepanov, D. M. Sedlovets, *Mater. Res. Express* **2019**, *6*, 055317; b) D. M. Sedlovets, M. V. Shuvalov, Y. V. Vishnevskiy, V. T. Volkov, I. I. Khodos, O. V. Trofimov, V. I. Korepanov, *Mater. Res. Bull.* **2013**, *48*, 3955; c) X.-F. Zhang, Q. Xi, J. Zhao, *J. Mater. Chem.* **2010**, *20*, 6726.
- [20] S. Santucci, L. Lozzi, L. Ottaviano, *Handbook of Surfaces and Interfaces of Materials*, Elsevier, Amsterdam, **2001**, p. 239.
- [21] D. Zheng, Z. Gao, X. He, F. Zhang, L. Liu, *Appl. Surf. Sci.* **2003**, *211*, 24.
- [22] L. Ottaviano, S. Di Nardo, L. Lozzi, M. Passacantando, P. Picozzi, S. Santucci, *Surf. Sci.* **1997**, *373*, 318.
- [23] U. Mazur, M. Leonetti, W. A. English, K. Hips, *J. Phys. Chem. B* **2004**, *108*, 17003.
- [24] J. Åhlund, K. Nilson, J. Schiessling, L. Kjeldgaard, S. Berner, N. Mårtensson, C. Puglia, B. Brena, M. Nyberg, Y. Luo, *J. Chem. Phys.* **2006**, *125*, 034709.
- [25] a) L. Ottaviano, L. Lozzi, F. Ramondo, P. Picozzi, S. Santucci, *J. Electron Spectrosc. Relat. Phenom.* **1999**, *105*, 145; b) A. Ghosh, J. Fitzgerald, P. G. Gassman, J. Almlöf, *Inorg. Chem.* **1994**, *33*, 6057.
- [26] D. Roy, N. M. Das, N. Shakti, P. Gupta, *RSC Adv.* **2014**, *4*, 42514.

- [27] W. Ji, T.-X. Wang, X. Ding, S. Lei, B.-H. Han, *Coord. Chem. Rev.* **2021**, *439*, 213875.
- [28] a) N. Han, Y. Wang, L. Ma, J. Wen, J. Li, H. Zheng, K. Nie, X. Wang, F. Zhao, Y. Li, *Chem* **2017**, *3*, 652; b) J. Chen, J. Li, W. Liu, X. Ma, J. Xu, M. Zhu, Y.-F. Han, *Green Chem.* **2019**, *21*, 6056.
- [29] a) M. Zhu, R. Ye, K. Jin, N. Lazouski, K. Manthiram, *ACS Energy Lett.* **2018**, *3*, 1381; b) S. Vijay, W. Ju, S. Brückner, S.-C. Tsang, P. Strasser, K. Chan, *Nat. Catal.* **2021**, *4*, 1024.
- [30] J. Choi, P. Wagner, S. Gambhir, R. Jalili, D. R. MacFarlane, G. G. Wallace, D. L. Officer, *ACS Energy Lett.* **2019**, *4*, 666.
- [31] a) X. M. Hu, M. H. Rønne, S. U. Pedersen, T. Skrydstrup, K. Daasbjerg, *Angew. Chem. Int. Ed.* **2017**, *56*, 6468; b) Z. Meng, J. Luo, W. Li, K. A. Mirica, *J. Am. Chem. Soc.* **2020**, *142*, 21656.

Manuscript received: July 10, 2023

Accepted manuscript online: August 2, 2023

Version of record online: August 11, 2023